Density Functional Theory Model for Adsorption-Induced Deformation of Mesoporous Materials with Non-Convex Pore Geometry

Andrei L. Kolesnikov,[*,†,‡] Yury A. Budkov,[¶,§] and Gennady Y. Gor[*,‡]

†*Institut für Nichtklassische Chemie e.V., Permoserstr. 15, 04318 Leipzig, Germany*

‡*Otto H. York Department Chemical and Materials Engineering, New Jersey Institute of Technology, University Heights, Newark, NJ 07102, USA*

¶*School of Applied Mathematics, Tikhonov Moscow Institute of Electronics and Mathematics, National Research University Higher School of Economics, Tallinskaya st. 34, 123458 Moscow, Russia*

§*G.A. Krestov Institute of Solution Chemistry of the Russian Academy of Sciences, Academicheskaya st., 1, 153045 Ivanovo, Russia*

E-mail: kolesnikov@inc.uni-leipzig.de; gor@njit.edu

Abstract

Adsorption of fluids in nanoporous media causes mechanical stresses which results in deformation. This phenomenon is ubiquitous and its magnitude depends on the pore size and geometry. Adsorption and adsorption-induced deformation are typically modeled in slit-shape or convex (cylindrical or spherical) pores. However, many porous materials are composed of spherical grains, so that the pores are formed by the intergranular spaces between the convex solid surfaces. Here we present a first theoretical study of adsorption-induced deformation in non-convex pores, in particular we studied the templated mesoporous carbons. The model is based on classical density functional theory within the local density approximation applied to the description of hard sphere interactions. We predict the adsorption isotherms and solvation pressure isotherms for nitrogen adsorption in CMK-3 carbons. The shape of adsorption isotherm matches the shape of experimental isotherm. The predicted solvation pressure isotherms are qualitatively different from the solvation pressure isotherms in cylindrical pores. We attribute this difference to formation of liquid bridges between the adjacent rods. Our results suggest that adsorption-induced deformation in materials with non-convex pores cannot be predicted within the existing models. These results may shed some light on understanding adsorption-induced deformation of consolidated granular media.

 This article appeared in Kolesnikov, A; Budkov, Y. A.; Gor, G. Y. "Density Functional Theory Model for Adsorption-Induced Deformation of Mesoporous Materials with Non-Convex Pore Geometry" *J. Phys. Chem. C* 2020, 124, 37, 20046-20054, and may be found at DOI: 10.1021/acs.jpcc.0c03963

Introduction

Adsorption-induced deformation is a strain of a material as a result of the gas or liquid adsorption on its surface. This phenomenon is ubiquitous for all nanoporous materials, where the surface-to-volume ratio is high.[1,2] Adsorption-induced deformation has been shown as a promising mechanism for several applications, such as sensing and actuating devices[3–6] and material characterization.[7–10]

The last decade brought significant progress in experimental studies of this phenomenon, including in situ dilatometry,[11] small angle X-ray scattering,[12–14] small angle neutron scattering,[15,16] etc. The results of these measurements give strain isotherms – deformation measured as a function of vapor pressure. Those isotherms show various trends: expansion, contraction, or sequential combination of both. The values of strain vary in the range from tenths of percentage to the decades of percentage.[1] Recent literature has been also rich with theoretical works on adsorption-induced deformation. One can separate them in two groups: macroscopic/phenomenological models,[10,17–19] based on quantities that could be measured in an experiment and describe the whole sample, and microscopic models based on molecular simulation techniques,[9,20–25] or classical density functional theory.[8,26–30]

Up to now the focus in investigations of adsorption-induced deformation was mainly on the materials with planar or convex pores, for example templated silica or porous glasses. Simple geometrical representations of pores (planar, cylindrical or spherical) were sufficient in order to reproduce not only adsorption isotherms, but also strain isotherms.[17,26,31,32] However, there is a class of materials, whose pores substantially differ from "simple" ones. Namely, their porous body consists of convex, predominantly non-porous, parts. Important examples are opals, the pore structure of which are formed by non-convex pores.[33,34] Some templated carbons also have non-convex pores and present a nice reference materials for studying adsorption-induced deformation,[35] such as inverse replica of SBA-15 silica, CMK-3 templated carbon,[36] which consists of hexagonally ordered rods holding together by thin interconnections .[37] The non-convex pore space leads to unusually broad hysteresis on nitrogen

adsorption isotherm.[35]

Recently, the monolithic templated carbon with hierarchical porous structure, and macroporous morphology was synthesized,[38,39] and proposed as a candidate for a double-layer electrode, where the complex structure provides enhanced transport through micro- and mesopores and high power density due to the presence of micropores.[40]

The experimental evidence of deformation of templated mesoporous carbons induced by electrosorption,[41] suggests that they will noticeably deform as a result of gas adsorption as well. However, to the best of our knowledge, neither experimental measurements nor modeling have been reported. Since the pore morphology in these materials is qualitatively different from typical porous materials, represented by slit, spherical and cylindrical pore models, the adsorption-induced deformation can be qualitatively different from the known models.[1]

The aim of the paper is to develop a thermodynamic model of adsorption-induced deformation of materials with non-convex pores, using CMK-3 like structure as an example. Most of currently existing adsorption models were developed to describe adsorption in "simple" porous geometries, such as slit, cylindrical and spherical geometry. However, the application of these models to the materials with non-convex pores can be used only as an estimation of the real behavior. Also, to the best of our knowledge, classical density functional theory (cDFT) approach for modeling adsorption has not been applied for the CMK-3 pore geometry, and therefore our manuscript is also the first to describe the adsorption isotherms in CMK-3 like materials, using cDFT.

Methods

Modeling of Adsorption in CMK-3 Type Materials

We model the adsorption and adsorption-induced deformation using the classical density functional theory (cDFT)[42] for the system of hexagonally arranged carbon rods (see Fig.

1). The cDFT has been used for over two decades for modeling adsorption, and gained success for its low computational cost as compared to molecular simulation techniques.[43] The equilibrium state of this system is determined by the minimum of the grand thermodynamic potential Ω of the system, represented as a functional of the fluid density $\rho(\mathbf{r})$ at fixed chemical potential μ of the reservoir

$$\Omega[\rho(\mathbf{r})] = F[\rho(\mathbf{r})] + \int \mathrm{d}\mathbf{r}\phi(\mathbf{r})\rho(\mathbf{r}) - \mu \int \mathrm{d}\mathbf{r}\rho(\mathbf{r}). \tag{1}$$

Here $F[\rho(\mathbf{r})]$ is the intrinsic Helmholtz free energy of the fluid, and $\phi(\mathbf{r})$ is the solid-fluid potential of interactions. The equilibrium fluid density profile is determined from the Euler-Lagrange equation:

$$\frac{\delta F[\rho(\mathbf{r})]}{\delta \rho(\mathbf{r})} - \mu + \phi(\mathbf{r}) = 0 \tag{2}$$

For an arbitrary pore geometry, numerical solution of Eq. 2 presents a significant computational challenge. However, if the pore has symmetries (slit-shaped, cylindrical or spherical) and the problem becomes one-dimensional, the solution of Eq. (2) is straightforward. There are several versions of cDFT, determined by the types of the functionals in Eq. (1), which differ in the complexity of implementation and the rigour of quantitative predictions. For example, the least complex approach, which yet gives qualitative predictions for modeling adsorption of simple fluids is the local density approximation (LDA).[42] LDA does not take into account short-range correlations between the fluid particles that is why the resulting density profiles does not have oscillation behavior. Currently, the most widely used cDFT versions are based on Tarazona's smoothed density functional theory[44] and fundamental measure theory (FMT)[45] (with its variations[46]), predicting the adsorption isotherms which are fully consistent with the predictions of molecular simulation.[47] However, the current system does not reduce to the one-dimensional problem, because the density profile is the 2D surface. Due to significant increase in the complexity of the problem and computational cost we will use simplified version of density functional, namely van der Waals (VdW) DFT.[48] It

is based on the local contribution from short-range hard-spheres interactions and non-local one from the attractive van der Waals interactions.

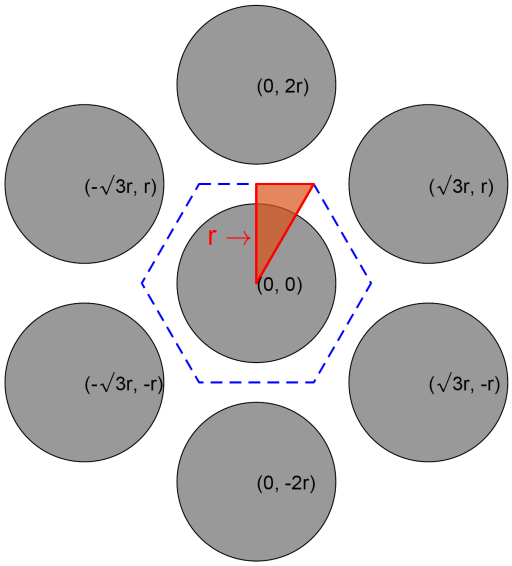

Figure 1: The porous system presents void space between carbon rods, arranged in the hexagonal tiling. The radii of the rod is R and the coordinates of the centers are given on the figure. The red triangle represent the geometry of unique part of the fluid density profile which is subject to minimization in the numerical procedure.

The total Helmholtz free energy is the sum of two contributions:

$$F = \mathcal{F}_{\text{id}} + \mathcal{F}_{\text{ex}}, \tag{3}$$

where $\mathcal{F}_{\text{id}}$ is the ideal part of free energy and $\mathcal{F}_{\text{ex}}$ is the excess one. Ideal part is purely local:

$$\mathcal{F}_{\text{id}} = k_{\text{B}}T \int \mathrm{d}\mathbf{r}\rho(\mathbf{r})[\ln(\Lambda^3\rho(\mathbf{r})) - 1], \tag{4}$$

where k_{B} is the Boltzmann constant and T is temperature. The excess part of free energy, in its turn, also consists of two contributions – hard sphere short range interaction between fluid molecules ($\mathcal{F}_{\text{HS}}$) and attraction tail between them ($\mathcal{F}_{\text{att}}$). The first one is taken from

scaled-particle theory and corresponds to the bulk limit of Helmholtz free energy of FMT:

$$\mathcal{F}_{\mathrm{HS}} = k_{\mathrm{B}}T \int \mathrm{d}\mathbf{r}\rho(\mathbf{r}) \left[-\ln(1-\eta) + \frac{3\eta}{1-\eta} + \frac{3\eta^2}{2(1-\eta)^2} \right], \tag{5}$$

where $\eta = \rho(\mathbf{r}) d_{\mathrm{HS}}^3 \pi/6$ is also position-dependent packing fraction, where d_{HS} is the hard sphere diameter. The attraction tail is treated via perturbation approach in the mean-field approximation:

$$\mathcal{F}_{\mathrm{att}} = \frac{1}{2} \int \mathrm{d}\mathbf{r}_1 \rho(\mathbf{r}_1) \int \mathrm{d}\mathbf{r}_2 \rho(\mathbf{r}_2) \phi_{\mathrm{ff}}(|\mathbf{r}_1 - \mathbf{r}_2|), \tag{6}$$

with $\phi_{\mathrm{ff}}(r)$ being the attraction part of the inter-particle potential of interactions, which is taken in the form of the square well potential

$$\phi_{\mathrm{ff}}(r) = \begin{cases} 0, & r < d_{\mathrm{HS}} \\ -\epsilon_{\mathrm{ff}}, & d_{\mathrm{HS}} \leq r \leq \lambda\ d_{\mathrm{HS}} \\ 0, & r > \lambda\ d_{\mathrm{HS}} \end{cases}$$

where λ is the range parameter and ϵ_{ff} is the depth of square well.

The solid-fluid interaction potential is determined by the geometry of the system (Fig. 1), and it is what makes the CMK-3 system qualitatively different from slit, cylindrical and spherical pores. The solid-fluid interactions are represented by Lennard-Jones potential. In the present system, due to symmetry one can identify the "unit cell" around each rod, it is represented by the dashed hexagon in the Fig. 1. Moreover, the unique part of fluid density profile is smaller and represented by the red triangle on the same figure. Thus, if we find the solution in the unique part we know the total density profile. Also, the solution symmetry imposes the boundary conditions on the density profile. The external potential is taken as a sum over seven rods from Fig. 1:

$$\phi(\mathbf{r}) = \sum_{i=1}^{7} \phi_i(\sqrt{(x-x_i)^2 + (y-y_i)^2}) \tag{7}$$

where ϕ_i is the potential due to only one rod with coordinates of the center (x_i, y_i):[49]

$$\begin{aligned}\phi_i(r) &= \epsilon_{\mathrm{sf}}\rho_{\mathrm{s}}\sigma_{\mathrm{sf}}^2\pi^2\left[\frac{63}{32}\frac{R}{r}\frac{\sigma_{\mathrm{sf}}^{10}}{r^{10}\left(1-\left(\frac{R}{r}\right)^2\right)^{10}}F\left(-\frac{9}{2},-\frac{9}{2};1;\left(\frac{R}{r}\right)^2\right)\right.\\ &- \left. 3\frac{R}{r}\frac{\sigma_{\mathrm{sf}}^4}{r^4\left(1-\left(\frac{R}{r}\right)^2\right)^4}F\left(-\frac{3}{2},-\frac{3}{2};1;\left(\frac{R}{r}\right)^2\right)\right] \qquad (8)\end{aligned}$$

The equilibrium density profile satisfy Eq. 2, which can be solved via well known Piccard iterative procedure (the comprehensive description can be found elsewhere, see, for instance,[46]). In order to apply the iterative method we need to express density profile explicitly:

$$\rho(\mathbf{r}) = \rho_{\mathrm{b}}\exp\left(\beta\left[\mu_{\mathrm{ex,b}} - \frac{\delta\mathcal{F}_{\mathrm{HS}}}{\delta\rho(\mathbf{r})} - \int \mathrm{d}\mathbf{r_1}\rho(\mathbf{r}_1)\phi_{\mathrm{ff}}(|\mathbf{r}_1-\mathbf{r}|) - \phi(\mathbf{r})\right]\right), \qquad (9)$$

where ρ_{b} is the bulk density, $\mu_{\mathrm{ex,b}}$ is the excess part of chemical potential in the bulk, $\beta = 1/k_{\mathrm{B}}T$ and $\delta\mathcal{F}_{\mathrm{HS}}/\delta\rho(\mathbf{r})$ is the variation of hard-sphere contribution, which within LDA is the part of local excess chemical potential.

Parameterization of the Model

In order to determine the unknown potentials of fluid-fluid interactions, we fit them from the experimental densities of coexisting phases, surface tension, and saturation pressure at 77 K. The consistent equations for the bulk fluid are obtained by the following substitution $\rho(\mathbf{r}) \to \rho_{\mathrm{b}}$ and simultaneously $\phi(\mathbf{r}) = 0$. Here we present two equations, namely defining pressure and chemical potential of the bulk fluid:

$$P = k_{\mathrm{B}}T\rho_{\mathrm{b}}\frac{1+\eta_{\mathrm{b}}+\eta_{\mathrm{b}}^2}{(1-\eta_{\mathrm{b}})^3} + \frac{1}{2}B\rho_{\mathrm{b}}^2, \qquad (10)$$

$$\mu = \ln(\Lambda^3\rho_{\mathrm{b}}) + k_{\mathrm{B}}T\left[-\ln(1-\eta_{\mathrm{b}}) + \eta\frac{14-13\eta_{\mathrm{b}}+5\eta_{\mathrm{b}}^2}{2(1-\eta_{\mathrm{b}})^2}\right] + B\rho_{\mathrm{b}}, \qquad (11)$$

with $B = -4\pi/3 d_{\mathrm{HS}}^3 \epsilon_{\mathrm{ff}}(\lambda^3 - 1)$ and bulk packing fraction $\eta_{\mathrm{b}} = \pi d_{\mathrm{HS}}^3 \rho_{\mathrm{b}}/6$. The extended discussion of the fitting procedure, surface tension calculations, and the choice of solid-fluid interaction potentials is presented in SI. Here we summarize the resulting parameters in the Table 1:

Table 1: The used parameters are represented in the table.

$\epsilon_{\mathrm{ff}}/k_{\mathrm{B}}$ [K]	λ [-]	d_{HS} [nm]	$\epsilon_{\mathrm{sf}}/k_{\mathrm{B}}$ [K]	σ_{sf} [nm]	ρ_{s} [nm^{-2}]	σ_{c} [nm]
151	1.5[50]	0.355	74.23[51]	0.3494[51]	38.19	0.34[52]

The parameters spatial arrangement of the carbon rods were chosen in order to approximate the real mesoporous structure of the sample, namely $r = 5\,\mathrm{nm}$ and $R \simeq 3.72\,\mathrm{nm}$.[53] We normalize the adsorbed amount in the CMK-3 by the surface area of the effective solid (which is "visible" for the fluid molecules)

$$\Gamma_{\mathrm{CMK}} = \frac{1}{2\pi(R + \sigma_{\mathrm{c}}/2)} \left[\int_{S_{\mathrm{HEX}}} \rho(\mathbf{r}) d\mathbf{r} - \rho_{\mathrm{b}}(S_{\mathrm{HEX}} - \pi(R + \sigma_{\mathrm{c}}/2)^2) \right], \tag{12}$$

where S_{HEX} is the surface area of the hexagon on Fig. 1 and σ_{c} is an effective diameter of carbon atom.

Modeling of Deformation

In the paper we consider only one source of the deformation, specifically an elongation of virtual springs connecting the rods of equal length L. The springs connect each rod with six nearest neighbors and distributed along the axial direction with a density per rod length ρ_{spr}. Thus, the elastic energy of the system, where we neglect the effects of the boundary, is:

$$F_{\mathrm{el}} = \frac{3}{2} M \rho_{\mathrm{spr}} L \kappa (h - h_0)^2, \tag{13}$$

where κ is the elastic constant of the spring, M is the number of the rods, h and h_0 are the actual and reference spring length. Also, we assume that κ does not depend on the

temperature.

Let us consider the system composing of CMK-3 material immersed in the reservoir of fluid molecules. The equilibrium of the system is defined by the following thermodynamic potential corresponding to the $\mu - P - T$ ensemble, i.e.

$$\Delta G = F_{\mathrm{el}} + F_{\mathrm{ads}} - \mu_0 N + PV, \tag{14}$$

where F_{ads} is the Helmholtz free energy of the solid-fluid system in the volume of the sample V, P is the pressure in the reservoir and μ_0 is the chemical potential in the reservoir. In this equation we also neglect the excess contribution corresponding to the external surface of the whole sample. Applying the condition of the thermodynamic equilibrium – the equality of the chemical potential across the whole system the Gibbs thermodynamic potential can be rewritten as follows

$$\Delta G = F_{\mathrm{el}} + \Omega + PV, \tag{15}$$

with the grand thermodynamic potential $\Omega = F_{\mathrm{ads}} - \mu N$. The imposition of the above-mentioned condition only changes the path of equilibration, but not the final state, because during adsorption the chemical potential of the reservoir does not change. Minimizing the Eq. 15 with respect to the spring distance h, using Eq. 13 we obtain the following equation:

$$\frac{\sqrt{3}\rho_{\mathrm{spr}}\kappa}{D_{\mathrm{s}} + h_0}(h - h_0) = -P - \frac{\sqrt{3}}{3ML(D_{\mathrm{s}} + h_0)}\frac{\mathrm{d}\Omega}{\mathrm{d}h}, \tag{16}$$

where $D_{\mathrm{s}} = 2\ R_{\mathrm{s}}$. We approximated the derivative of the grand thermodynamic potential and the volume of the system at the point $h = h_0$ with the fixed bulk chemical potential and temperature. Thus, we neglect the coupling between adsorption and adsorption-induced deformation.[2,18] It will contribute rather small error to the final result at sufficiently large elastic constant (weak deformation). The derivative of the grand thermodynamic potential is taken numerically using the above described density functional approach in the following way: we change the distance between all rods by the value of 0.04 nm and used a simple

two-point estimation. As far as we neglected the excess contribution to the free energy from the sample surface, the density profile can be considered as a solution far from the boundary of the sample.

Results

Prior to calculating adsorption and adsorption-induced deformation for the CMK-3 type pores, we test our model on well-studied cylindrical pores.[1,10,17,27] First, we compare the behavior of the solvation term in Eq. 16 (the second term which we denote as f_{CMK}) with the similar for a cylindrical pore. Solvation pressure produced by cylindrical pores was previously defined as:[17]

$$f_{\mathrm{cyl}} = -\frac{1}{2\pi L R_{\mathrm{c}}} \frac{\mathrm{d}\Omega}{\mathrm{d}R_{\mathrm{c}}}, \tag{17}$$

where the derivative taken at constant temperature and chemical potential. Here, R_{c} is the radius of cylinder – distance from the pore to the center of the first layer of carbon atoms. We used the standard adsorption potential for cylindrical pore geometry,[54] which is the result of an integration over all atoms in the layer.

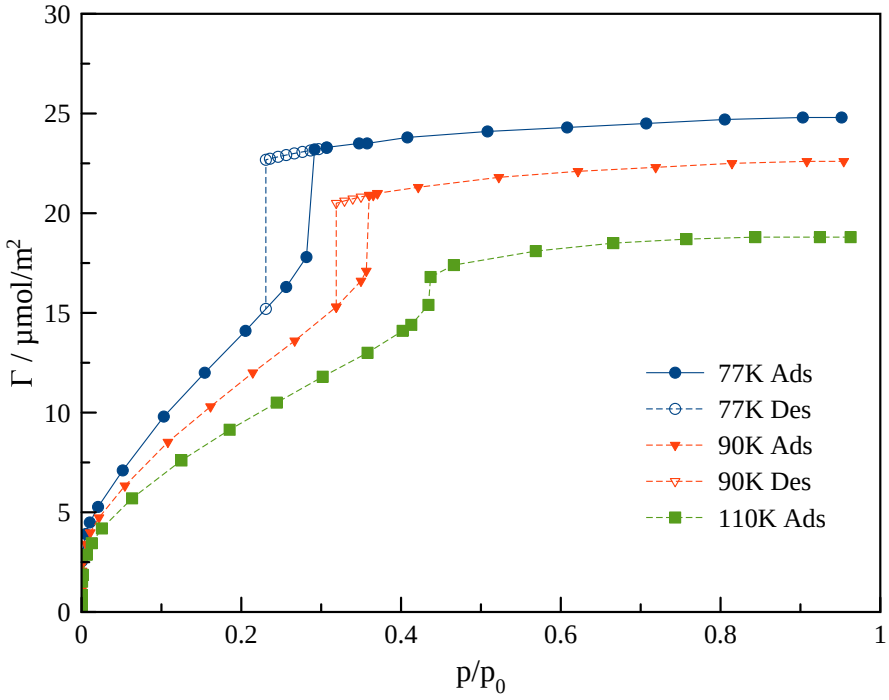

Figure 2: Calculated isotherms in cylindrical pore with $R_c = 2\,\text{nm}$ at 77 K, 90 K and 110 K. Adsorption and desorption branches were calculated for all three temperatures, except 110 K where the difference between the positions of condensation and equilibrium evaporation transitions is minor.

Also, we used the same cDFT, with its local/non-local contributions and parameters of interactions as for the description of the CMK-3 material. We focus here on the description of these calculation, due to the fact that the comprehensive description of the cDFT implementation can be found elsewhere.[46,48,55,56] The pore radius were chosen as a radius of the inscribed circle between three carbon rods $R_c = (2-\sqrt{3})R + h/\sqrt{3} \simeq 2\,\text{nm}$. An excess adsorbed amount per surface area is defined with respect to some reference pore[55] with the same effective diameter of the carbon atom σ_c.

Figures 2 and 3 present the calculated excess adsorbed amount in cylindrical pore and in CMK-3 material at three different temperatures 77 K, 90 K and 110 K. We calculated both adsorption and desorption branches, assuming that the desorption takes place in the equilibrium fashion, i.e. the capillary evaporation transition is calculated from the equality of grand-thermodynamic potentials of two phases.

Fig. 2 shows that the isotherms for cylindrical pores are Type IVa isotherms with H1 type hysteresis[57] – they have two regions with a capillary condensation/evaporation transition between them. Thus the predictions of our model are consistent with more rigorous cDFT models.[55] The isotherms for CMK-3 material shown on Fig. 3 look qualitatively different. They demonstrate three different stages of adsorption: multilayer adsorption, bridge formation and condensation. The formation of liquid bridges is clearly seen from the density profiles shown in Fig. 4. The capillary condensation occurs as a first order phase transition at all studied temperatures. On the other hand, bridging transition at 110 K occurs smoothly that could be a sign that critical temperature of the bridging transition is distinguished from the critical temperature of the condensation in the particular system.

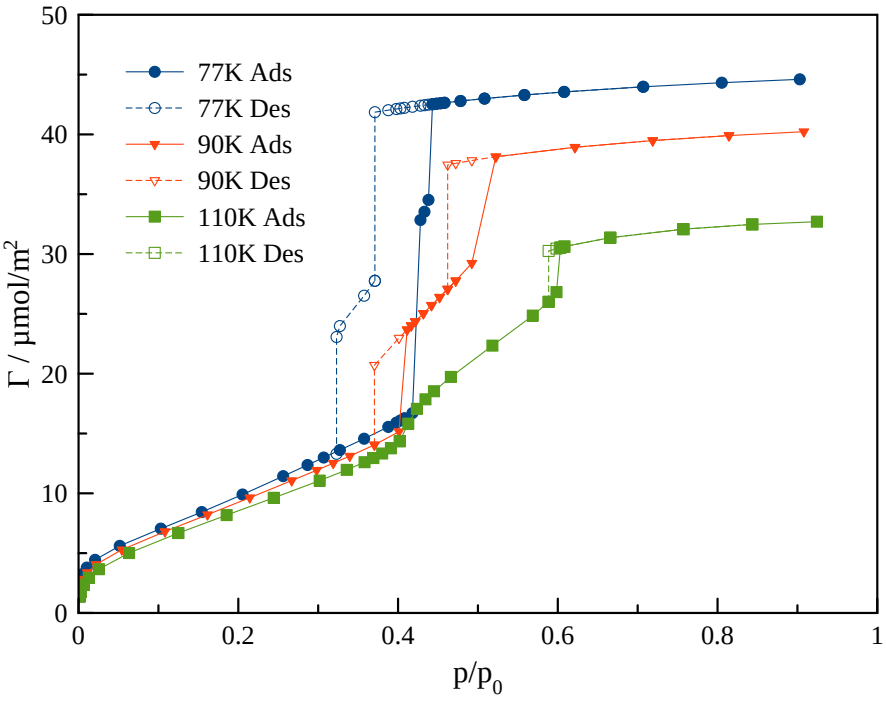

Figure 3: Calculated isotherms of CMK-3 material at 77 K, 90 K and 110 K. Adsorption and desorption branches were calculated for all there temperatures.

We treated the hysteresis observed in our calculations for CMK-3 system in the conventional way: adsorption branch corresponds to the delayed condensation and desorption branch – to the equilibrium transition. Hysteresis at 77 K for CMK-3 does not have bridging

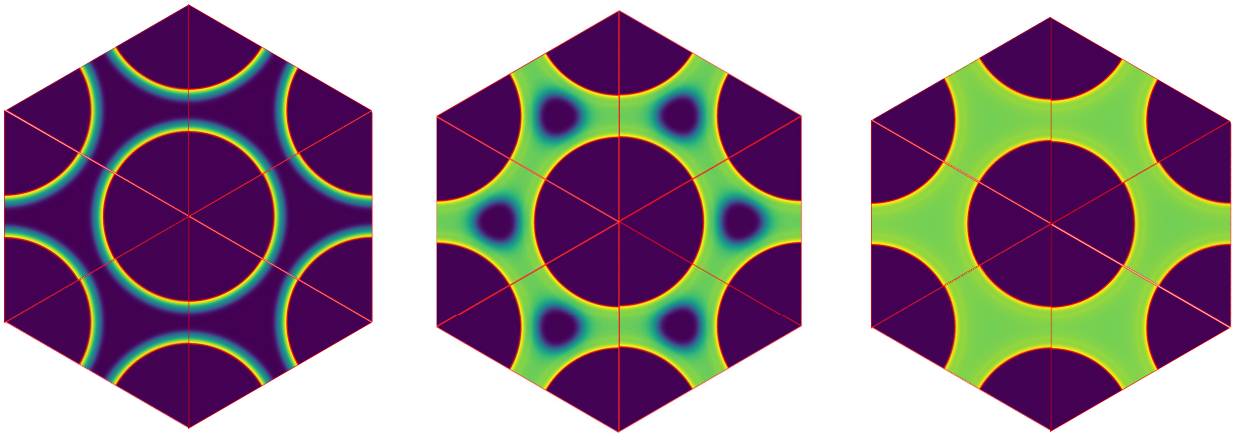

Figure 4: The three stages during adsorption process in CMK-3 material at 77 K are depicted. There are, from left to right, multilayer adsorption ($p/p_0 \simeq 0.3$), bridging stage ($p/p_0 \simeq 0.43$) and condensed stage ($p/p_0 \simeq 0.9$).

stage on the desorption path, in contrast, there are two hysteresis loops at 90 K. The first one corresponds to bridge formation and the second one to the capillary condensation. The hysteresis in cylindrical pores shifted to higher relative pressures with temperature increase. CMK-3 isotherms demonstrate in general the similar behavior, however the position of the bridge formation remains almost unaltered. Also, Fig. 4 demonstrate the density profiles at 77 K for the mentioned stages, from left to right, multilayer, bridging and condensed. As one can see, there is some amount of volume which is not filled with condensate during the bridging process.

Figures 6 and 7 present the solvation pressure isotherms calculated for cylindrical pores and CMK-3 material respectively. The results for cylindrical pores are in general consistent with the solvation pressure calculated previously in the QSDFT and DBdB frameworks for a nitrogen adsorption on silica.[27] The difference occurs at low relative pressures ($\simeq 10^{-6}$), namely minor minimum, which could be attributed to the different values of solid-fluid parameters of interactions or, which is more probable, it is the artifact of the local nature of short-range repulsive contribution (see Eq. 5). The solvation pressure isotherms for CMK-3 qualitatively differ from the isotherms for the cylindrical pores. The generated solvation pressure prior the bridge formation is almost negligible and decreases significantly in the

bridging regime. It is worth noting that at temperatures 77 K and 90 K the solvation pressure undergoes step-wise behavior at the positions of bridge formation and capillary condensation. However, there is only one step on solvation pressure at 110 K – during capillary condensation and continuous decrease during bridge formation.

Discussion

Although gas adsorption in materials composed of parallel rods, such as CMK-3 carbons, is frequently described assuming the cylindrical pore model,[58,59] the adsorption process in the such system can be qualitatively different. Our density functional theory model shows two phase transitions (Fig. 4) from multilayer adsorption to bridged phase and then to the filled pore. Note that this is consistent with the macroscopic model from Dobbs and Yeomans.[60] Authors studied the adsorption in the system of axially aligned cylinders and found that, during initial adsorption stages, liquid bridges can be formed between the cylinders. A recent extension of Dobbs and Yeomans model[53] demonstrated the similar bridge formations in the CMK-3-like material. Fig. 5 demonstrates the adsorption and solvation pressure isotherms at 77 K for CMK-3 geometry with the inter-cylinder distance equal to $h = 3.5$ nm. The hysteresis becomes much broader comparing to the results for $h = 2.5$ nm and the solvation pressure prior to the capillary condensation even fewer. The bridging transition is not seen neither on the adsorption nor on the desorption branch. However, the absence of the transition can be related to the numerical procedure, because for the desorption calculations we started from the filled pore state. Thus, the solution corresponding to the bridge could be overlooked. Nevertheless, the disappearance of the bridge transition on the adsorption branch confirms the results presented in Refs.[53,60] As the DFT model used in the current paper approximates the fluid-fluid interactions with the square-well potential, one should not expect full quantitative agreement with the experimental data,[59] or the data obtained using molecular simulations utilizing the Lennard-Jones potential.[49,61] However, the qualitative

agreement of the shape of the adsorption isotherms with both experimental[59] and recent molecular simulation data (taking into account the peculiarities of CMK-3 geometry[49]) is clearly seen.

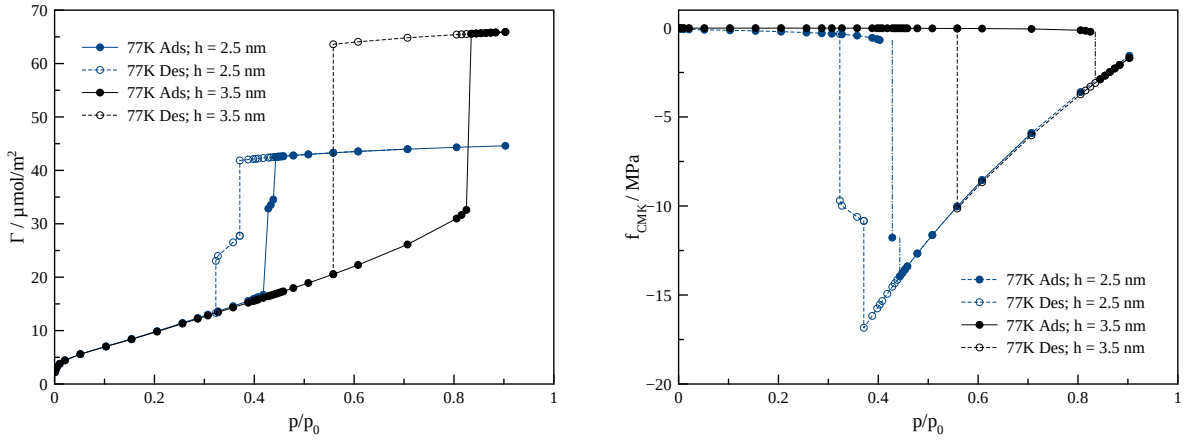

Figure 5: The adsorption (left) and solvation pressure (right) isotherms for two CMK-3 with different inter-cylinder distance (2.5 nm and 3.5 nm) at 77 K are depicted. Dash-dotted lines indicate the positions and approximate the magnitude of solvation pressure change along the adsorption branch. Due to the discontinuities in the vicinity of the capillary condensation, more rigorous calculations are problematic.

In addition to this qualitative difference in adsorption isotherms, the solvation pressure differs even more from the cylindrical pore model. The solvation pressure prior bridged transition is almost zero in comparison with the maximum one. The similar absence of disjoining force was observed in hybrid molecular dynamics/Monte Carlo simulation,[23] where the authors studied the deformation of planar pore. Both in work[23] and here we observed the absence of the Bangham's expansion typical for cylindrical pores.[18,62] The detailed discussion of the determination of the spring constants and strain magnitude is given at the end of the present section.

The solvation pressure in the bridging regime can be approximated with a good accuracy by means of the following simple equation:

$$f_{\mathrm{br}}(p/p_0) \simeq C - \gamma/R, \tag{18}$$

where C is an independent on relative pressure vertical shift and R is the average radius of the liquid-vapor interface during the bridge formation. The position of the interface was estimated by the contour curve on the 2D density distribution with the level equal to the average density on the binodal at given temperature. In fact, the second term in Eq. 18 approximates the contribution of capillary forces. The comparison between Eq. 18 and cDFT is presented on the Fig. 7 and is satisfactory at relative pressures near to capillary condensation. The deviation near to evaporation transition can be addressed to the complex form of the liquid-vapor interface at lower p/p_0, which cannot be described by one principle radius of curvature. Similar bridge transitions have been discussed between two spherical and cylindrical particles.[50] Also, the authors proposed qualitatively different behavior of solvation pressure during bridge formation, namely jump-wise, rounded and critical.

The behavior of the solvation force in the filled regime is instructive to study in the simplified mean-field model, where fluid density is constant and fluid interacts only with the nearest carbon rod. That type of model was previously used in the description of polymer swelling/shrinkage (coil-globule transition) in two component mixtures, see for instance[63,64] and citation therein.

Despite the significant difference in the system considered here and in Refs.,[63,64] in both systems intrusion of low molecular weight molecules leads to the dimensional change of the host (a polymer coil or a solid body). That is why we expect that models developed for the polymer solutions could contribute, at least limited, to the present study.

Within the mean-field model the following thermodynamic potential has a minimum in the adsorption process:

$$\Omega(\rho) = V k_{\mathrm{B}} T \rho \left(\ln(\Lambda^3 \rho) - 1\right) + F_{\mathrm{ex}} + M \rho \phi_0 - \mu_{\mathrm{b}} \rho V, \tag{19}$$

where μ_{b} is fixed and equal to the chemical potential of the fluid far from the sample, ρ is the density of the adsorbed fluid, ϕ_0 is the integrated potential of interaction between fluid

molecule and the carbon rod (the integration was taken over the whole volume of the system due to fast decay of the potential Eq. 8) and F_{ex} is defined by Eqs. 4–6 in the bulk limit. Using ρ as an order parameter and minimizing Eq. 19 with respect to it, we get the equality condition for chemical potentials: $\mu(\rho) + M/V\phi_0 = \mu_{\mathrm{b}}$. Thus, thermodynamic potential at equilibrium is identical to the grand thermodynamic potential and can be rewritten as: $\Omega = -VP(\mu_{\mathrm{b}} - M\phi_0/V)$, with $V = V_{\mathrm{tot}} - V_{\mathrm{solid}}$ being the free volume between the rods. The solid volume is defined as a volume of rods with effective diameter, which were taken as $R_{\mathrm{s}} + 0.8\sigma_{\mathrm{sf}}$, which corresponds to the position where fluid density reaches zero in cDFT calculations. Thus, we can obtain the solvation pressure by Eq. 16 and expand it near the saturation chemical potential in the bulk (μ_b^{sat}):

$$f_{\mathrm{mf}} \simeq f_{\mathrm{mf}}(\rho(\mu_b^{\mathrm{sat}})) + \left(\rho + \rho^2\beta_T\frac{M\phi_0}{V}\right)\Bigg|_{\mu_{\mathrm{b}}=\mu_b^{\mathrm{sat}}} \delta\mu_{\mathrm{b}}, \tag{20}$$

where the first term is the value of the solvation pressure at $p/p_0 = 1$ and β_T is the isothermal compressibility. That equation is similar to a widely-used estimation of solvation pressure within framework of incompressible fluid [1,10,17] ($f \simeq C + \rho_{\mathrm{l}}RT\ln(p/p_0)$, where ρ_{l} is the molar density of bulk liquid at coexistence and C is independent on p/p_0 parameter. That equation is used to fit the experimental strain isotherms measured on mesoporous materials. In fact, Eq. 20 reproduces almost the same slope as the incompressible approximation at 77 K, where we can neglect the effects of the non-ideality in the chemical potential. However, non-ideal correction will be significant at higher temperatures. Also, the expression in the brackets reproduces values of ρ_{l} with acceptable accuracy 29 933 mol/m^3(28 832 mol/m^3) at 77 K, 27 198 mol/m^3 (26 595 mol/m^3) at 90K and 23 155 mol/m^3 (22 184 mol/m^3) at 110 K. Experimental values from NIST data base are presented in the brackets and the error does not exceed 5%. In addition, Eq. 20 demonstrates only minor temperature dependence and in order to compare it directly with cDFT results, we added a constant shift. Despite this, our mean-field model gives qualitatively correct value of $f_{\mathrm{mf}}(\rho(\mu_{\mathrm{b}}^{\mathrm{sat}}))$, for instance, at 77 K

it is equal to $\simeq -2.12\,\mathrm{MPa}$.

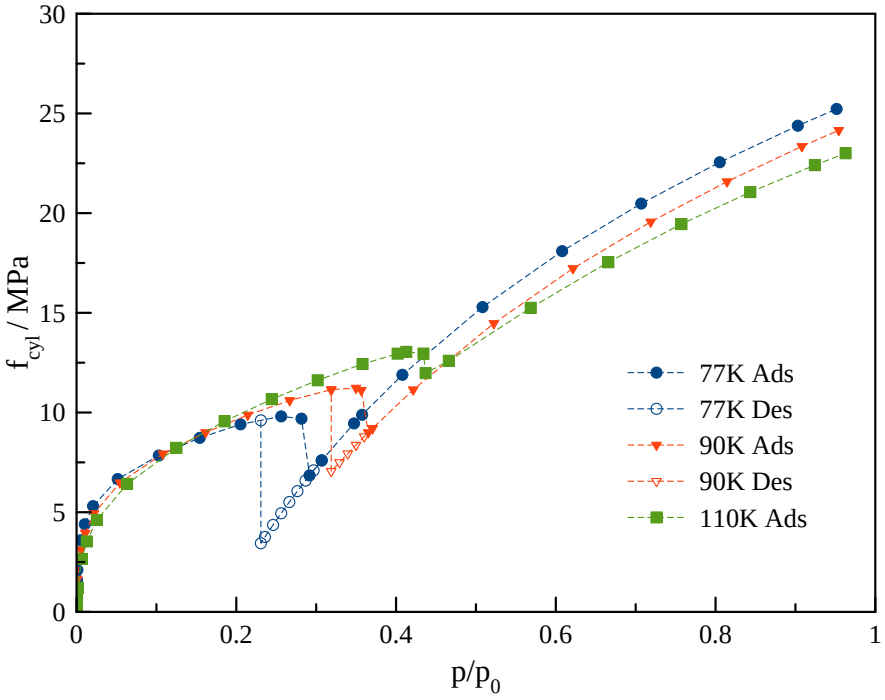

Figure 6: Calculated solvation pressure isotherms in cylindrical pore with $R_c = 2\,\mathrm{nm}$ at 77 K, 90 K, and 110 K. Adsorption and desorption branches were calculated for all there temperatures, except 110 K where the difference between the positions of condensation and equilibrium evaporation transitions is minor.

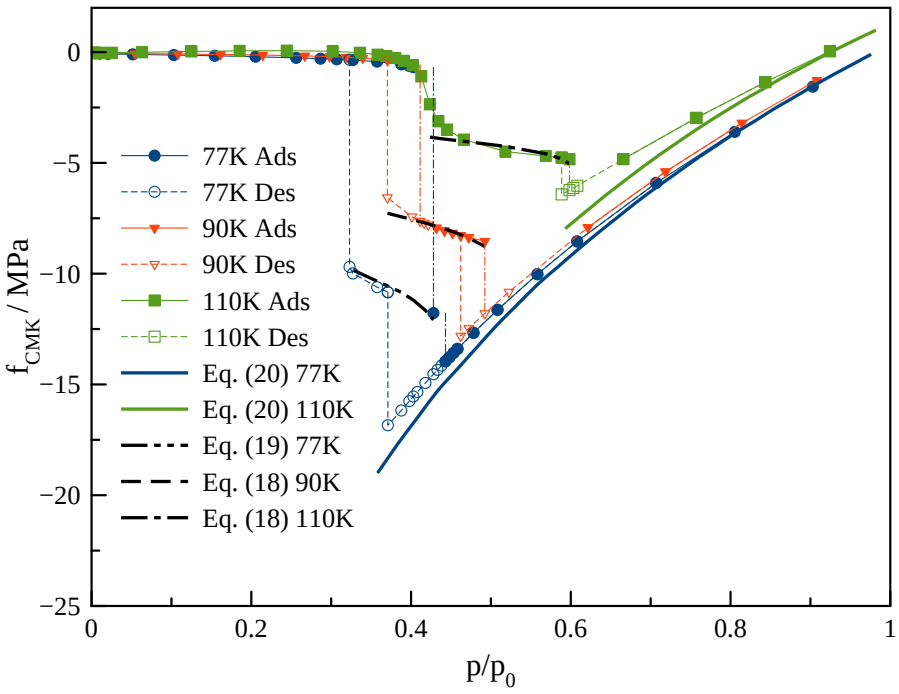

Figure 7: Calculated solvation pressure isotherms of CMK-3 material at 77 K, 90 K, and 110 K. Adsorption and desorption branches were calculated for all three temperatures. The solid lines correspond to the mean-field estimates by Eq. 20 shifted vertically. Dashed and chain lines correspond to the approximations made by means of Eq. 18 with constant shift for 90 K and 110 K, respectively. Dash-dotted lines indicate the positions and approximate the magnitude of solvation pressure change along the adsorption branch. Due to the discontinuities in the vicinity of the capillary condensation, more rigorous calculations are problematic.

It is important to contrast the difference in adsorption isotherms and the difference in solvation pressure isotherms between the cylindrical pores and a system of rods. The isotherms shown in Fig. 3, while having two phase transitions and two hysteresis loops, have similar shape to the isotherms in Fig. 2. An adsorption isotherm originating from the materials with bi-modal distribution of cylindrical pores can look the same as a CMK-3 isotherm. Thus, adsorption measurements do not allow to reveal the difference between the two pore geometries. However, since the solvation pressure isotherms look qualitatively different for the two geometries, solvation pressure isotherms could be employed to extract additional information for pore characterization.

To the best of our knowledge, there are no literature data regarding the adsorption-

induced deformation of CMK-3, hence we will estimate the spring constant from the typical values ($10^{-3}-10^{-2}$) of adsorption-induced strain of another porous materials[1,11,17] (including carbons) at high relative pressures. The strain values of electrosorption-induced deformation of porous carbon with hierarchical structure[41] also correlate with that range. Following our assumption that the distance between the virtual springs is greater than h, we use $\rho_{\mathrm{spr}} \simeq 0.05\,\mathrm{nm}^{-1}$. Now, we consider the case when the cross section area of the body that is perpendicular to the carbon rods can be estimated by a^2, where a is the side of a square. Then, linear elongation is $\epsilon \simeq \frac{h-h_0}{D_{\mathrm{s}}+h_0}$ and can be estimated from the solvation pressure as $\epsilon = f_{\mathrm{CMK}}/\sqrt{3}\rho_{\mathrm{spr}}\kappa$ (here we neglect the contribution from external pressure). Using the value of f_{CMK} equal to 10 MPa - typical for bridging regime, where the maximum solvation pressure is achieved, we estimate that the spring constant is between $11-115\,\mathrm{J/m^2}$. The silica template for the CMK-3 type material should have second porous network in the range of micro- or small mesopores. As stated above, virtual springs correspond to interconnections, appeared as an inverse replica of these pores. Thus, assuming that they have cylindrical shape, we can recalculate κ to the Young modulus $E = \kappa h_0/A$, where A is the area of a cylindrical rod. The latter is the result of the comparison between the strain-stress relation for the homogeneous axial deformation of the cylinder and the force arising in the virtual spring with the same length. Using the area of 1.5 nm circle, we can estimate the range of Young modulus of the interconnections as $\simeq 4-40\,\mathrm{GPa}$. On the other hand, knowing the Young's modulus of the interconnections and their geometry one can evaluate the spring elastic constant. Also, it can be accessed by the fitting of the experimental strain data using Eq. 16. However, both of these procedures require additional estimates of the axial interconnection density.

Conclusion

Adsorption-induced deformation takes place in all in a porous materials, but theoretical studies typically focus on model pores with either slit, cylindrical, or spherical pore geometry. We presented the first theoretical study considering adsorption-induced deformation in the system with non-convex pore geometry. As an example of such system we considered CMK-3 carbon – a system of hexagonally ordered cylindrical rods. We used the classical density functional theory to model adsorption of nitrogen in this system. Using the adsorption isotherms we calculated the solvation pressure, which is the driving force for the adsorption-induced deformation. We compared our predictions for the solvation pressure to the solvation pressure isotherms in cylindrical pores calculated using the same model. Our comparison revealed a qualitative difference between the two geometries. In cylindrical pores prior to the capillary condensation the solvation pressure monotonically increases, corresponding to expansion of the sample (Bangham's law); in CMK-3 the solvation pressure remains in this region zero, thus not causing deformation before the capillary condensation. This result may have significant implications for the analysis of experimental data on the materials with non-convex for geometry, in addition to CMK-3 carbons, considered here, such materials include e.g. silica colloidal crystals and other materials in which the pores are formed by the spaces between the spherical grains.

Acknowledgments

This work was supported by a postdoc fellowship of the German Academic Exchange Service (DAAD). Y.B. thanks Russian Foundation for Basic Research Grant No 18-29-06008 for financial support. G.Y.G. acknowledges the support from the National Science Foundation (CBET-1944495).

Supporting Information

Details of fluid-fluid and solid-fluid parameters of interactions as noted in the text. Tabulated data corresponding to cylindrical and CMK-3 pores.

References

(1) Gor, G. Y.; Huber, P.; Bernstein, N. Adsorption-Induced Deformation of Nanoporous Materials – a Review. *Appl. Phys. Rev.* **2017**, *4*, 011303.

(2) Vandamme, M. Coupling between Adsorption and Mechanics (and vice versa). *Curr. Opin. Chem. Eng.* **2019**, *24*, 12–18.

(3) Ganser, C.; Fritz-Popovski, G.; Morak, R.; Sharifi, P.; Marmiroli, B.; Sartori, B.; Amenitsch, H.; Griesser, T.; Teichert, C.; Paris, O. Cantilever Bending Based on Humidity-actuated Mesoporous Silica/Silicon Bilayers. *Beilstein J. Nanotechnol.* **2016**, *7*, 637–644.

(4) Van Opdenbosch, D.; Fritz-Popovski, G.; Wagermaier, W.; Paris, O.; Zollfrank, C. Moisture-Driven Ceramic Bilayer Actuators from a Biotemplating Approach. *Adv. Mater.* **2016**, *28*, 5235–5240.

(5) Boudot, M.; Elettro, H.; Grosso, D. Converting Water Adsorption and Capillary Condensation in Usable Forces with Simple Porous Inorganic Thin Films. *ACS Nano* **2016**, *10*, 10031–10040.

(6) Zhao, Q.; Dunlop, J. W.; Qiu, X.; Huang, F.; Zhang, Z.; Heyda, J.; Dzubiella, J.; Antonietti, M.; Yuan, J. An Instant Multi-responsive Porous Polymer Actuator Driven by Solvent Molecule Sorption. *Nat. Commun.* **2014**, *5*, 1–8.

(7) Balzer, C.; Cimino, R. T.; Gor, G. Y.; Neimark, A. V.; Reichenauer, G. Deformation of

Microporous Carbons during N2, Ar, and CO2 Adsorption: Insight from the Density Functional Theory. *Langmuir* **2016**, *32*, 8265–8274.

(8) Ustinov, E.; Do, D. Effect of Adsorption Deformation on Thermodynamic Characteristics of a Fluid in Slit Pores at Sub-critical Conditions. *Carbon* **2006**, *44*, 2652–2663.

(9) Kowalczyk, P.; Balzer, C.; Reichenauer, G.; Terzyk, A. P.; Gauden, P. A.; Neimark, A. V. Using in-situ Adsorption Dilatometry for Assessment of Micropore Size Distribution in Monolithic Carbons. *Carbon* **2016**, *103*, 263–272.

(10) Kolesnikov, A.; Georgi, N.; Budkov, Y. A.; Möllmer, J.; Hofmann, J.; Adolphs, J.; Gläser, R. Effects of Enhanced Flexibility and Pore Size Distribution on Adsorption-induced Deformation of Mesoporous Materials. *Langmuir* **2018**, *34*, 7575–7584.

(11) Balzer, C.; Wildhage, T.; Braxmeier, S.; Reichenauer, G.; Olivier, J. P. Deformation of Porous Carbons upon Adsorption. *Langmuir* **2011**, *27*, 2553–2560.

(12) Günther, G.; Prass, J.; Paris, O.; Schoen, M. Novel Insights into Nanopore Deformation Caused by Capillary Condensation. *Phys. Rev. Lett.* **2008**, *101*, 086104.

(13) Balzer, C.; Morak, R.; Erko, M.; Triantafillidis, C.; Hüsing, N.; Reichenauer, G.; Paris, O. Relationship Between Pore Structure and Sorption-Induced Deformation in Hierarchical Silica-Based Monoliths. *Zeitschrift für Physikalische Chemie* **2015**, *229*, 1189–1209.

(14) Balzer, C.; Waag, A. M.; Gehret, S.; Reichenauer, G.; Putz, F.; Hüsing, N.; Paris, O.; Bernstein, N.; Gor, G. Y.; Neimark, A. V. Adsorption-Induced Deformation of Hierarchically Structured Mesoporous Silica – Effect of Pore-Level Anisotropy. *Langmuir* **2017**, *33*, 5592–5602.

(15) Bahadur, J.; Melnichenko, Y.; He, L.; Contescu, C.; Gallego, N.; Carmichael, J. SANS Investigations of CO2 Adsorption in Microporous Carbon. *Carbon* **2015**, *95*, 535–544.

(16) Ludescher, L.; Morak, R.; Balzer, C.; Waag, A. M.; Braxmeier, S.; Putz, F.; Busch, S.; Gor, G. Y.; Neimark, A. V.; Hüsing, N. et al. In Situ Small-Angle Neutron Scattering Investigation of Adsorption-Induced Deformation in Silica with Hierarchical Porosity. *Langmuir* **2019**, *35*, 11590–11600.

(17) Gor, G. Y.; Neimark, A. V. Adsorption-Induced Deformation of Mesoporous Solids. *Langmuir* **2010**, *26*, 13021–13027.

(18) Gor, G. Y.; Bernstein, N. Revisiting Bangham's Law of Adsorption-induced Deformation: Changes of Surface Energy and Surface Stress. *Phys. Chem. Chem. Phys.* **2016**, *18*, 9788–9798.

(19) Neimark, A. V.; Grenev, I. V. Adsorption-Induced Deformation of Microporous Solids: A New Insight from a Century-Old Theory. *J. Phys. Chem. C* **2020**, *124*, 749–755.

(20) Do, D.; Nicholson, D.; Do, H. Effects of Adsorbent Deformation on the Adsorption of Gases in Slitlike Graphitic Pores: A Computer Simulation Study. *J. Phys. Chem. C* **2008**, *112*, 14075–14089.

(21) Valenzuela, G. E.; Saavedra, J. H.; Rozas, R. E.; Toledo, P. G. Force Exerted by a Nanoscale Capillary Water Bridge between Two Planar Substrates. *Phys. Chem. Chem. Phys.* **2016**, *18*, 11176–11183.

(22) Diao, R.; Fan, C.; Do, D.; Nicholson, D. Monte Carlo Simulation of Adsorption-induced Deformation in Finite Graphitic Slit Pores. *J. Phys. Chem. C* **2016**, *120*, 29272–29282.

(23) Chen, M.; Coasne, B.; Guyer, R. A.; Derome, D.; Carmeliet, J. Molecular Simulation of Sorption-induced Deformation in Atomistic Nanoporous Materials. *Langmuir* **2019**, *35*, 7751–7758.

(24) Vekeman, J.; Sanches-Marin, J.; Sanches de Meras, A.; Garcia Cuesta, I.; Faginas-

Lago, N. Flexibility in the Graphene Sheet: The Influence on Gas Adsorption from Molecular Dynamics Studies. *J. Phys. Chem. C* **2019**, *123*, 28035–28047.

(25) Tesson, S.; Firoozabadi, A. Deformation and Swelling of Kerogen Matrix in Light Hydrocarbons and Carbon Dioxide. *J. Phys. Chem. C* **2019**, *123*, 29173–29183.

(26) Ravikovitch, P. I.; Neimark, A. V. Density Functional Theory Model of Adsorption Deformation. *Langmuir* **2006**, *22*, 10864–10868.

(27) Gor, G. Y.; Neimark, A. V. Adsorption-Induced Deformation of Mesoporous Solids: Macroscopic Approach and Density Functional Theory. *Langmuir* **2011**, *27*, 6926–6931.

(28) Grégoire, D.; Malheiro, C.; Miqueu, C. Estimation of Adsorption-induced Pore Pressure and Confinement in a Nanoscopic Slit Pore by a Density Functional Theory. *Continuum Mech. Thermodyn.* **2018**, *30*, 347–363.

(29) Hlushak, S. Heat of Adsorption, Adsorption Stress, and Optimal Storage of Methane in Slit and Cylindrical Carbon Pores Predicted by Classical Density Functional Theory. *Phys. Chem. Chem. Phys.* **2018**, *20*, 872–888.

(30) Guyer, R. A.; Kim, H. A. Theoretical Model for Fluid-solid Coupling in Porous Materials. *Phys. Rev. E* **2015**, *91*, 042406.

(31) Kowalczyk, P.; Furmaniak, S.; Gauden, P. A.; Terzyk, A. P. Carbon Dioxide Adsorption-induced Deformation of Microporous Carbons. *J. Phys. Chem. C* **2010**, *114*, 5126–5133.

(32) Emelianova, A.; Maximov, M. A.; Gor, G. Y. Solvation Pressure in Spherical Mesopores: Macroscopic Theory and Molecular Simulations. *AIChE Journal* **2020**, DOI: 10.1002/aic.16542.

(33) Galukhin, A.; Bolmatenkov, D.; Emelianova, A.; Zharov, I.; Gor, G. Y. Porous Structure of Silica Colloidal Crystals. *Langmuir* **2019**, *35*, 2230–2235.

(34) Maximov, M. A.; Galukhin, A. V.; Gor, G. Y. Pore-Size Distribution of Silica Colloidal Crystals from Nitrogen Adsorption Isotherms. *Langmuir* **2019**, *35*, 14975–14982.

(35) Jun, S.; Joo, S. H.; Ryoo, R.; Kruk, M.; Jaroniec, M.; Liu, Z.; Ohsuna, T.; Terasaki, O. Synthesis of New, Nanoporous Carbon with Hexagonally Ordered Mesostructure. *J. Am. Chem. Soc.* **2000**, *122*, 10712–10713.

(36) Jun, S.; Joo, S. H.; Ryoo, R.; Kruk, M.; Jaroniec, M.; Liu, Z.; Ohsuna, T.; Terasaki, O. Synthesis of New, Nanoporous Carbon with Hexagonally Ordered Mesostructure. *J. Am. Chem. Soc.* **2000**, *122*, 10712–10713.

(37) Solovyov, L. A.; Shmakov, A. N.; Zaikovskii, V. I.; Joo, S. H.; Ryoo, R. Detailed Structure of the Hexagonally Packed Mesostructured Carbon Material CMK-3. *Carbon* **2002**, *40*, 2477–2481.

(38) Taguchi, A.; Smått, J.-H.; Lindén, M. Carbon Monoliths Possessing a Hierarchical, Fully Interconnected Porosity. *Adv. Mater.* **2003**, *15*, 1209–1211.

(39) Putz, F.; Ludescher, L.; Elsaesser, M. S.; Paris, O.; Huesing, N. Hierarchically Organized and Anisotropic Porous Carbon Monoliths. *Chem. Mater.* **2020**,

(40) Koczwara, C.; Rumswinkel, S.; Hammerschmidt, L.; Salihovic, M.; Elsaesser, M. S.; Amenitsch, H.; Paris, O.; Huesing, N. Nanofibers versus Nanopores: A Comparison of the Electrochemical Performance of Hierarchically Ordered Porous Carbons. *ACS Appl. Energy Mater.* **2019**, *2*, 5279–5291.

(41) Koczwara, C.; Rumswinkel, S.; Prehal, C.; Jäckel, N.; Elsässer, M. S.; Amenitsch, H.; Presser, V.; Hüsing, N.; Paris, O. In Situ Measurement of Electrosorption-Induced Deformation Reveals the Importance of Micropores in Hierarchical Carbons. *ACS Appl. Mater. Interfaces* **2017**, *9*, 23319–23324.

(42) Hansen, J.-P.; McDonald, I. R. *Theory of Simple Liquids*; Academic Press, 2013.

(43) Gubbins, K. E.; Liu, Y.-C.; Moore, J. D.; Palmer, J. C. The Role of Molecular Modeling in Confined Systems: Impact and Prospects. *Phys. Chem. Chem. Phys.* **2011**, *13*, 58–85.

(44) Tarazona, P.; Marconi, U. M. B.; Evans, R. Phase Equilibria of Fluid Interfaces and Confined Fluids. *Mol. Phys.* **1987**, *60*, 573–595.

(45) Rosenfeld, Y. Free-energy Model for the Inhomogeneous Hard-sphere Fluid Mixture and Density-functional Theory of Freezing. *Phys. Rev. Lett.* **1989**, *63*, 980–983.

(46) Roth, R. Fundamental Measure Theory for Hard-sphere Mixtures: A Review. *J. Phys.: Condens. Matter* **2010**, *22*, 063102.

(47) Ravikovitch, P. I.; Vishnyakov, A.; Neimark, A. V. Density Functional Theories and Molecular Simulations of Adsorption and Phase Transitions in Nanopores. *Phys. Rev. E* **2001**, *64*, 011602.

(48) Henderson, D. *Fundamentals of Inhomogeneous Fluids*; CRC Press, 1992.

(49) Yelpo, V.; Cornette, V.; Toso, J. P.; López, R. H. Characterization of Nanostructured Carbon CMK-3 by means of Monte Carlo Simulations. *Carbon* **2017**, *121*, 106–113.

(50) Malijevský, A.; Parry, A. O. Bridging Transitions for Spheres and Cylinders. *Phys. Rev. E* **2015**, *92*.

(51) Lastoskie, C.; Gubbins, K. E.; Quirke, N. Pore Size Distribution Analysis of Microporous Carbons: A Density Functional Theory Approach. *J. Phys. Chem.* **1993**, *97*, 4786–4796.

(52) Ravikovitch, P. I.; Vishnyakov, A.; Russo, R.; Neimark, A. V. Unified Approach to Pore Size Characterization of Microporous Carbonaceous Materials from N2, Ar, and CO2 Adsorption Isotherms. *Langmuir* **2000**, *16*, 2311–2320.

(53) Ludescher, L.; Braxmeier, S.; Balzer, C.; Reichenauer, G.; Putz, F.; Hüsing, N.; Gor, G. Y.; Paris, O. Capillary Bridge Formation Between Hexagonally Ordered Carbon Nanorods. *Adsorption* **2020**, 1–16.

(54) Tjatjopoulos, G. J.; Feke, D. L.; Mann Jr, J. A. Molecule-micropore Interaction Potentials. *J. Phys. Chem.* **1988**, *92*, 4006–4007.

(55) Ravikovitch, P. I.; Vishnyakov, A.; Neimark, A. V. Density Functional Theories and Molecular Simulations of Adsorption and Phase Transitions in Nanopores. *Phys. Rev. E* **2001**, *64*, 011602.

(56) Landers, J.; Gor, G. Y.; Neimark, A. V. Density Functional Theory Methods for Characterization of Porous Materials. *Colloids Surf., A* **2013**, *437*, 3–32.

(57) Thommes, M.; Kaneko, K.; Neimark, A. V.; Olivier, J. P.; Rodriguez-Reinoso, F.; Rouquerol, J.; Sing, K. S. W. Physisorption of Gases, with Special Reference to the Evaluation of Surface Area and Pore Size Distribution (IUPAC Technical Report). *Pure Appl. Chem.* **2015**, *87*, 1051–1069.

(58) Joo, S. H.; Ryoo, R.; Kruk, M.; Jaroniec, M. Evidence for General Nature of Pore Interconnectivity in 2-dimensional Hexagonal Mesoporous Silicas Prepared Using Block Copolymer Templates. *J. Phys. Chem. B* **2002**, *106*, 4640–4646.

(59) Gor, G. Y.; Thommes, M.; Cychosz, K. A.; Neimark, A. V. Quenched Solid Density Functional Theory Method for Characterization of Mesoporous Carbons by Nitrogen Adsorption. *Carbon* **2012**, *50*, 1583–1590.

(60) Dobbs, H.; Yeomans, J. Capillary Condensation within an Array of Cylinders. *Mol. Phys.* **1993**, *80*, 877–884.

(61) Jain, S. K.; Pellenq, R. J.-M.; Gubbins, K. E.; Peng, X. Molecular Modeling and Ad-

sorption Properties of Ordered Silica-templated CMK Mesoporous Carbons. *Langmuir* **2017**, *33*, 2109–2121.

(62) Bangham, D.; Fakhoury, N. The Expansion of Charcoal accompanying Sorption of Gases and Vapours. *Nature* **1928**, *122*, 681–682.

(63) Budkov, Y. A.; Kiselev, M. Flory-type Theories of Polymer Chains under Different External Stimuli. *J. Phys.: Condens. Matter* **2017**, *30*, 043001.

(64) Budkov, Y. A.; Kolesnikov, A. Models of the Conformational Behavior of Polymers in Mixed Solvents. *Polymer Science, Series C* **2018**, *60*, 148–159.

Graphical TOC Entry